NANO · MICRO small
www.small-journal.com

In Situ Grown Single-Atom Cobalt on Polymeric Carbon Nitride with Bidentate Ligand for Efficient Photocatalytic Degradation of Refractory Antibiotics

Yang Yang, Guangming Zeng, Danlian Huang,* Chen Zhang,* Donghui He, Chengyun Zhou, Wenjun Wang, Weiping Xiong, Biao Song, Huan Yi, Shujing Ye, and Xiaoya Ren*

Semiconductor photocatalysis is a promising technology to tackle refractory antibiotics contamination in water. Herein, a facile in situ growth strategy is developed to implant single-atom cobalt in polymeric carbon nitride (pCN) via the bidentate ligand for efficient photocatalytic degradation of oxytetracycline (OTC). The atomic characterizations indicate that single-atom cobalt is successfully anchored on pCN by covalently forming the Co—O bond and Co—N bond, which will strengthen the interaction between single-atom cobalt and pCN. This single-atom cobalt can efficiently expand optical absorption, increase electron density, facilitate charge separation and transfer, and promote OTC degradation. As the optimal sample, Co(1.28%)—pCN presents an outstanding apparent rate constant for OTC degradation (0.038 min^{-1}) under visible light irradiation, which is about 3.7 times than that of the pristine pCN. The electron spin resonance (ESR) tests and reactive species trapping experiments demonstrate that the $^1O_2$, h^+, $•O_2^-$, and •OH are responsible for OTC degradation. This work develops a new way to construct single-atom-modified pCN and provides a green and highly efficient strategy for refractory antibiotics removal.

1. Introduction

Antibiotics contamination in water is becoming a severe environmental problem that threatens human public health security.[1] Oxytetracycline (OTC) is a typical tetracycline, which is widely used as a prophylactic antibiotic in agriculture and aquaculture.[2] Because of the limited absorption by animals after ingestion, large amounts of undigested OTC are released into the environment through feces or urine. The OTC discharged into water can adversely affect ecological systems by suppressing the growth of microorganisms, inducing the formation of antibiotic-resistant genes, and leading to other ecotoxicological effects.[3] Accordingly, highly efficient and convenient methods are demanded for the removal of residual OTC in water.

Semiconductor photocatalysis is a novel and desirable technology for the treatment of organic pollutants, which can directly utilize solar energy and does not require exogenous chemical reagents or electrical energy.[4] Polymeric carbon nitride (pCN), as a metal-free organic semiconductor, has drawn tremendous attention due to its favorable band structure, environmental benignity, earth abundance, and excellent thermal and chemical stability.[5] Since the pioneering work reported in 2009 by Wang et al.,[6] pCN has been extensively utilized in photocatalytic applications, such as water splitting, CO_2 reduction, artificial photosynthesis, and environmental remediation.[7] Nevertheless, pristine pCN suffers from limited visible light absorption, low electronic conductivity, rapid charge carrier recombination behavior, and relatively few surface active sites, leading to very poor photocatalytic activity.

Within the last decade, various strategies, including heteroatom doping, heterojunction construction, and nanostructural engineering, have emerged to effectively resolve these troubles to enhance the photocatalytic performance of pCN.[8] Among them, introducing metal species into the pCN framework has stimulated much interest, as it can modulate the bandgap structure, extend the light absorption range, accelerate charge transfer, as well as provide more active sites.[9] More interestingly, the presence of electron-rich "nitrogen pot" in pCN would provide an ideal site for metal incorporation.[10] Cobalt-based materials have been attractive in photocatalysis recently owing to their low toxicity, high abundance, and low cost.[11] In general, cobalt was introduced into pCN structure in the form of nanoparticles (e.g., metallic cobalt, CoO, Co_3O_4, and CoP), and activity of the photocatalytic reactions was improved.[12]

Dr. Y. Yang, Prof. G. Zeng, Prof. D. Huang, Prof. C. Zhang, D. He, Dr. C. Zhou, Dr. W. Wang, Prof. W. Xiong, Dr. B. Song, Dr. H. Yi, Dr. S. Ye, Dr. X. Ren
College of Environmental Science and Engineering
Key Laboratory of Environmental Biology and Pollution Control (Hunan University)
Ministry of Education
Changsha 410082, P. R. China
E-mail: zgming@hnu.edu.cn; huangdanlian@hnu.edu.cn; zhangchen@hnu.edu.cn

The ORCID identification number(s) for the author(s) of this article can be found under https://doi.org/10.1002/smll.202001634.

DOI: 10.1002/smll.202001634

Unfortunately, the photocatalytic performances are still poor because only the atoms exposed on the surface of nanoparticles can participate in the reactions.[13] Therefore, how to increase the atom utilization efficiency of nanoparticles is the key issue.

Recently, uniformly anchoring single atom onto the pCN network via coordination bonds has been a research frontier in photocatalysis, owing to the maximum metal utilization.[14] Moreover, single-atom cobalt dispersed in pCN could greatly accelerate charge separation by the chemical bonding, and hence significantly improve the photocatalytic activity. For instance, Liu and co-workers designed a single Co_1–P_4 site confined on pCN through a pyrolysis reaction and a following phosphidation route.[15] This single Co site could efficiently restrain charge recombination and prolong carrier lifetime, and promote adsorption and activation of water molecular. As a result, this Co_1–phosphide/pCN composite photocatalyst presented a superior photocatalytic H_2 evolution rate of 410.3 μmol h^{-1} g^{-1} under simulated sunlight irradiation. Cao and co-workers successfully grafted single-atom cobalt on pCN in the form of Co_1–N_4 site by the method of atomic layer deposition.[16] The existence of coordinated donor nitrogen could assist the formation of key hydride intermediate on active Co center in the single Co_1–N_4 site, resulting in accelerated H—H coupling and enhanced H_2 production. Besides, Huang and co-workers achieved superior CO production with a turnover number of >200 on the process of photocatalytic CO_2 reduction under visible light irradiation ($\lambda > 420$ nm), by dispersing single Co^{2+} site on pCN through a simple deposition method, to improve the photocatalytic activity and promote the selective formation of CO.[17] However, in these studies, single-atom cobalt was generally incorporated into pCN by the postloading method, which would weaken the interfacial contact between the Co atom and pCN and reduce the stability of the composite. In addition, the postloading method was a multistep process, which would increase the complexity and cost of practical application. Accordingly, it is urgent to develop a simple method for the implantation of single-atom cobalt in pCN to significantly improve the photocatalytic performance.

In this work, we develop a facile in situ growth strategy to implant single-atom cobalt in pCN by the bidentate ligand. The atomic characterizations demonstrate that single-atom cobalt is successfully immobilized on pCN by covalently forming a Co—O bond and a Co—N bond. The Co—O bond and Co—N bond act as the links through which the interaction between single-atom cobalt and pCN is strengthened. Anchoring single-atom cobalt onto pCN not only extends optical absorption in the visible region but also accelerates photogenerated charge carrier separation, increases electron density, and facilitates electron transfer. These positive effects endow the single-atom cobalt incorporated pCN (Co–pCN) with superior photocatalytic activity for OTC degradation under visible light irradiation.

2. Results and Discussion

The Co–pCN is synthesized via an in situ keto–enol cyclization process of urea and cobalt(II) acetylacetonate to implant single-atom cobalt in pCN framework by the bidentate ligand, as shown in **Figure 1**a. First is the formation of 2-hydroxy-4,6-dimethylpyrimidine (HDMP) and tri-*s*-triazine ring, which are originated from the cyclization of acetylacetone with urea and the polymerization of urea, respectively. Then a bimolecular condensation occurs between the HDMP and tri-*s*-triazine ring. Finally, a single-atom cobalt-implanted pCN is generated through the chelation of hydroxyl group and nitrogen lone pair on HDMP with the Co^{2+}.

Solid-state ^{13}C nuclear magnetic resonance (NMR) spectra are utilized to analyze the carbon species of the samples. As shown in Figure 1b, the two carbon peaks at 165 and 157 ppm are obviously observed on pCN, which can be assigned to the C_1 (CN_3) and C_2 ($CN_2(NH_x)$) carbons, respectively.[18] During the cyclization and condensation process, the HDMP will be generated and incorporated into the pCN framework. Figure S1 (Supporting Information) demonstrates that the pure HDMP owns four distinct peaks at 181, 161, 157, and 108 ppm. Nevertheless, because of the formation of self-assembled structures between pyrimidine derivatives, the only peak that can be determined is 108 ppm, corresponding the C_3 (CC_2) carbon.[19] As for Co(1.28%)–pCN (Figure 1c), the two prominent peaks are detected at 165 and 157 ppm, similar to the spectrum of pCN. However, no obvious peaks of HDMP can be observed on Co(1.28%)–pCN due to the paramagnetic effect of Co. Thus, the solid-state ^{13}C NMR spectrum of acetylacetone-modified pCN (aa-PCN) is detected to verify the incorporation of HDMP. As shown in Figure 1d, the aa-pCN presents a new peak located at 90 ppm, which can be ascribed to the Cγ (CC_3) *para* to the hydroxyl group of HDMP. Compared to the pure HDMP, this peak is downshifted because the carbon is in a more electron-rich environment. These results indicate the successful implantation of HDMP into the pCN framework, which will provide both oxygen and nitrogen ligands as the efficient and strong coordination center for the Co atoms.

The crystal structures of the samples are characterized by X-ray diffraction (XRD) and presented in Figure 1e. Two characteristic peaks at 13.0° and 27.5° in pCN can be assigned to the (100) and (200) crystal planes, representing the intralayer repeated packing of tri-*s*-triazine units and the interlayer stacking of graphite-like materials, respectively.[20] In comparison with pCN, it is clear that the (100) peak disappears and the (002) peak becomes weaker and broader with increasing the Co content in Co–pCN. This is mainly due to the distortion of the planar structure around the Co centers in Co–pCN. Raman spectra are then used to confirm the difference of frameworks on pCN and Co–pCN (Figure 1f). A series of characteristic peaks belonging to pCN can be detected in the all samples. The peaks observed at 707 and 975 cm^{-1} correspond to the in-plane bending and the symmetric *N*-breathing mode of tri-*s*-triazine, and those at 1100–1700 cm^{-1} correspond to the disordered graphitic C—N vibrations.[21] This shows that the basic framework of pCN is well maintained in Co–pCN. From pCN to Co–pCN, the intensity of Raman signals is gradually weakened, which is ascribed to the formation of disordered structure around the Co centers. The microstructures of pCN and Co–pCN are further investigated by attenuated total reflectance Fourier transform infrared (ATR-FTIR) spectra. As shown in Figure 1g, both pCN and Co–pCN exhibit the feature peaks at around 810, 1200–1600, and 3000–3300 cm^{-1}, corresponding to the breathing mode of tri-*s*-triazine rings, stretching mode of C—N heterocycles, and

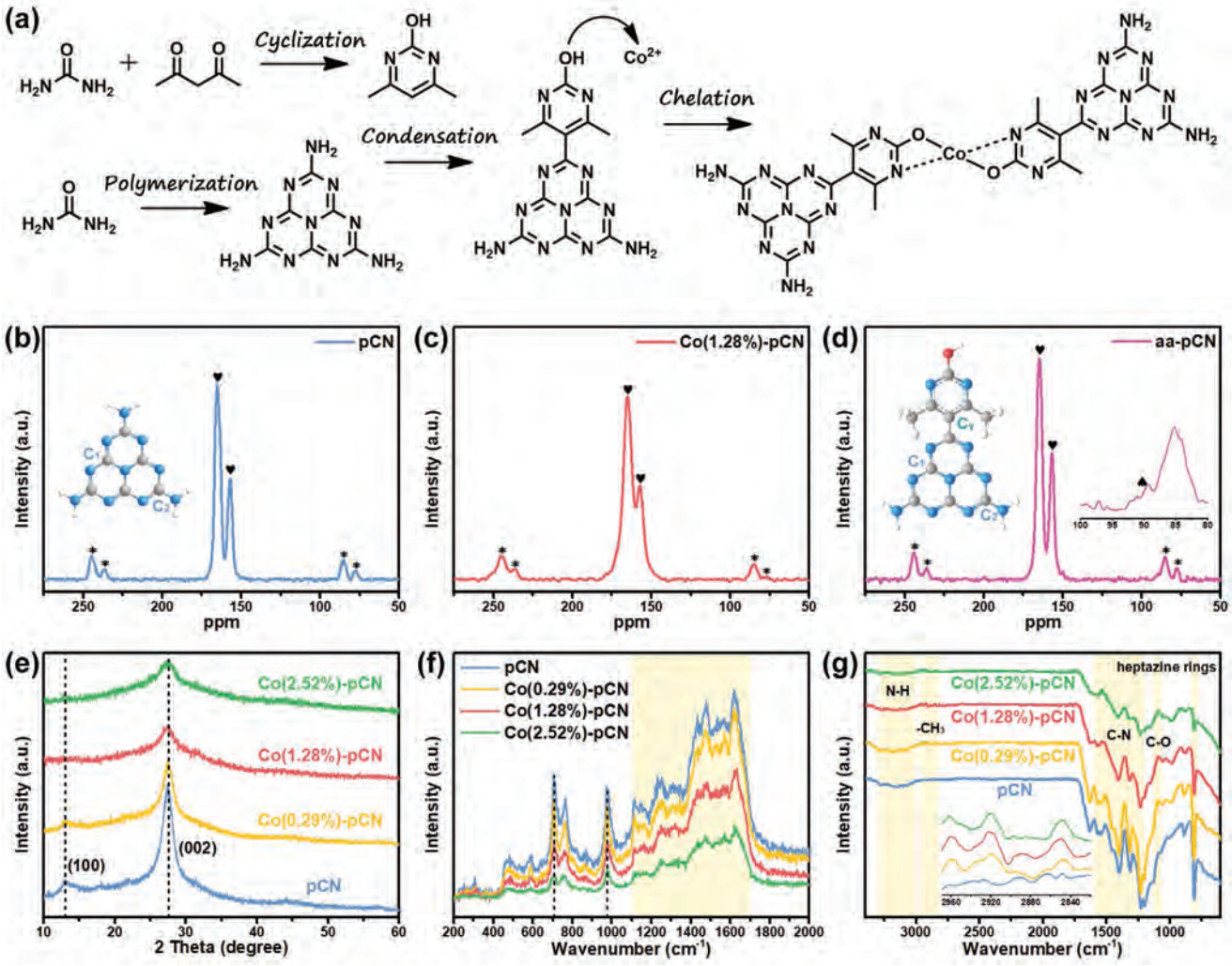

Figure 1. a) The proposed synthetic process of Co–pCN. Solid-state ^{13}C NMR spectra for b) pCN, c) Co(1.28%)–pCN, and d) aa-pCN (the symbols of *, ♥, and ♠ indicate the spinning sidebands of solid-state ^{13}C NMR spectra, the characteristic peaks of pCN, and the characteristic peaks of HDMP, respectively. e) XRD patterns, f) Raman spectra, and g) ATR-FTIR spectra of the samples.

N—H stretching vibrations, respectively.[22] This demonstrates that the Co–pCN still keeps the basic structure of pCN, which is in agreement with the Raman results. Compared to pCN, these peaks of Co–pCN are gradually getting weaker as the amount of Co increases due to the localized disorder structures around the Co centers. In addition, the intensity of C—O stretching at 1062–1134 cm^{-1} increases from pCN to Co–pCN owing to the incorporation of HDMP.[23] Meanwhile, new peaks emerge at 2820–2970 cm^{-1} in Co–pCN, which is ascribed to the stretching vibration of $-CH_3$ in HDMP.[24] Moreover, N_2 adsorption–desorption isotherms are used to measure the Brunauer–Emmett–Teller (BET) surface areas of the samples. As exhibited in Figure S2a (Supporting Information), all the samples present type IV adsorption curves, manifesting that they are mesoporous materials. The pore size distributions of them (Figure S2b, Supporting Information) also verify this result. The BET surface area is determined to be 68.76 $m^2 g^{-1}$ for Co(1.28%)–pCN, which is similar than that of pCN (72.13 $m^2 g^{-1}$), indicating that the surface area effect for the photocatalytic activity can be ignored.

The morphologies of pCN and Co(1.28%)–pCN are observed by scanning electron microscopy (SEM) and transmission electron microscopy (TEM). The SEM image in **Figure 2**a shows that pCN has a blocky-stacked structure. Compare to pCN, the morphology of Co(1.28%)–pCN is transferred to distorted and curled structure (Figure 2b) because the cobalt chelating pyrimidine derivative restrains the extension of tri-*s*-triazine units. For TEM images, the pCN exhibits the structure of layered silk-like sheets with wrinkles (Figure 2c), while Co(1.28%)–pCN displays a structure consisting of curly sheets (Figure 2d). No accumulation of nanoparticles or nanoclusters can be observed on the surface of Co(1.28%)–pCN. To confirm the distribution of the Co species, aberration-corrected high-angle-annular-dark-field scanning transmission electron microscopy (HAADF-STEM) characterization is performed. As displayed in Figure 2e, the HAADF-STEM image exhibits abundant bright dots, which are in atomic size, as highlighted by the red circles. Those bright dots correspond to the Co atoms, which are uniformly implanted in the pCN support, indicating

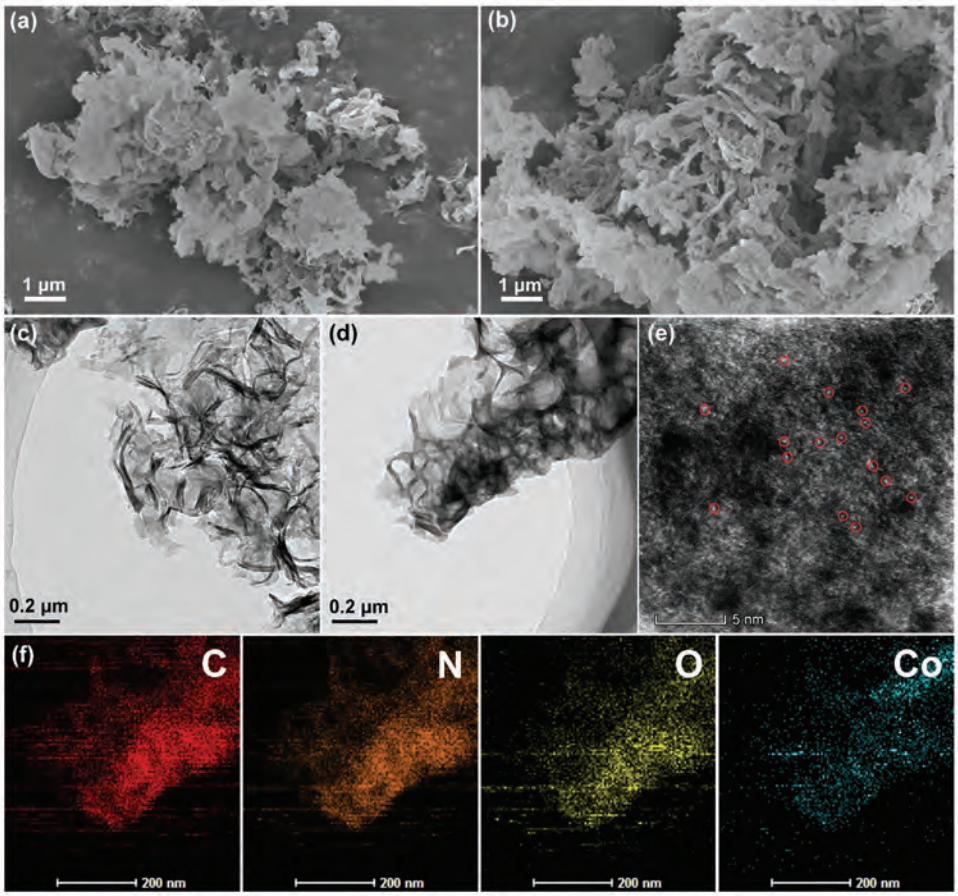

Figure 2. SEM images of a) pCN and b) Co(1.28%)–pCN. TEM images of c) pCN and d) Co(1.28%)–pCN. e) HADDF-STEM image and f) EDS elemental mapping images of Co(1.28%)–pCN.

that cobalt predominantly exists in the form of single atoms. The energy-dispersive X-ray spectroscopy (EDS) elemental mapping images (Figure 2f) further reveal that the Co atoms are homogeneously distributed on the pCN support. Therefore, these results demonstrate that Co species are mainly dispersed as isolated atoms on the pCN nanosheets.

To determine the electronic structure and coordination, X-ray absorption near-edge structure (XANES) and extended X-ray absorption fine structure (EXAFS) spectroscopy at the Co K-edge are recorded. As shown in **Figure 3**a, the absorption-edge position of Co(1.28%)–pCN is close to that of CoO and is located between the Co foil and Co_3O_4, demonstrating that the valence state of Co is around +2. The formation of Co—O and Co—N bonds in Co(1.28%)–pCN is verified by Fourier transformed (FT) k^3-weighted $\chi(k)$ function. As exhibited in Figure 3b, a Co-ligand peak at ≈1.5 Å in Co(1.28%)–pCN is observed, which is apparently different from the Co—Co coordination peak at 2.2 Å in Co foil and the Co—O coordination peak at 1.7 Å in CoO, further demonstrating the atomically dispersed Co species.[25] The 1.5 Å FT peak is similar to Co—N bond of CoPc, but with slight differences, which may be caused by the Co—O coordination bond. To obtain the quantitative structural parameters of Co in the Co(1.28%)–pCN, a least-squares EXAFS curve fit is conducted, as displayed in Figure 3c and in Figure S3 and Table S1 (Supporting Information). These results indicate that the Co is likely to be coordinated with the O and N atoms, and the coordination number is determined to be 2.6 and 2.6 for Co—O and Co—N, respectively. The coordination structure is also confirmed by the optimized density functional theory (DFT) calculation model as the most thermodynamically stable structure can be formed when both O and N atoms of HDMP participate in the Co coordination, shown in Figure 3d.

Furthermore, X-ray photoelectron spectroscopy (XPS) spectra are used to investigate the surface chemical state of pCN and Co(1.28%)–pCN. As exhibited in Figure S4 (Supporting Information), C, N, O, and Co elements are all detected in Co(1.28%)–pCN, but there is no Co element appearing in pCN. The C 1s spectrum of pCN (**Figure 4**a) possesses three peaks at 288.3, 285.3, and 284.8 eV, which are corresponded to sp^2-hybridized carbon (N—C=N), sp^3-coordinated carbon (C—N), and pure graphitic species (C—C/C=C), respectively.[26] In comparison with pCN, the Co(1.28%)–pCN has a new peak at 287.1 eV and stronger peaks at 285.3 and 284.8 eV. The new peak located at 287.1 eV is ascribed to the C—O in HDMP.[27] And the increment in C—N and C—C/C=C intensity should be also attributed to the incorporation of HDMP. In N 1s spectrum of pCN (Figure 4b), three peaks at 400.9, 399.6, and 398.8 eV are owing to terminal $C—NH_x$ amino functions, $N—C_3$ groups of skeleton, and sp^2-bonded nitrogen in C=N—C, respectively.[28] For Co(1.28%)–pCN, the $N—C_3$ peak shifts to the higher binding energy because the

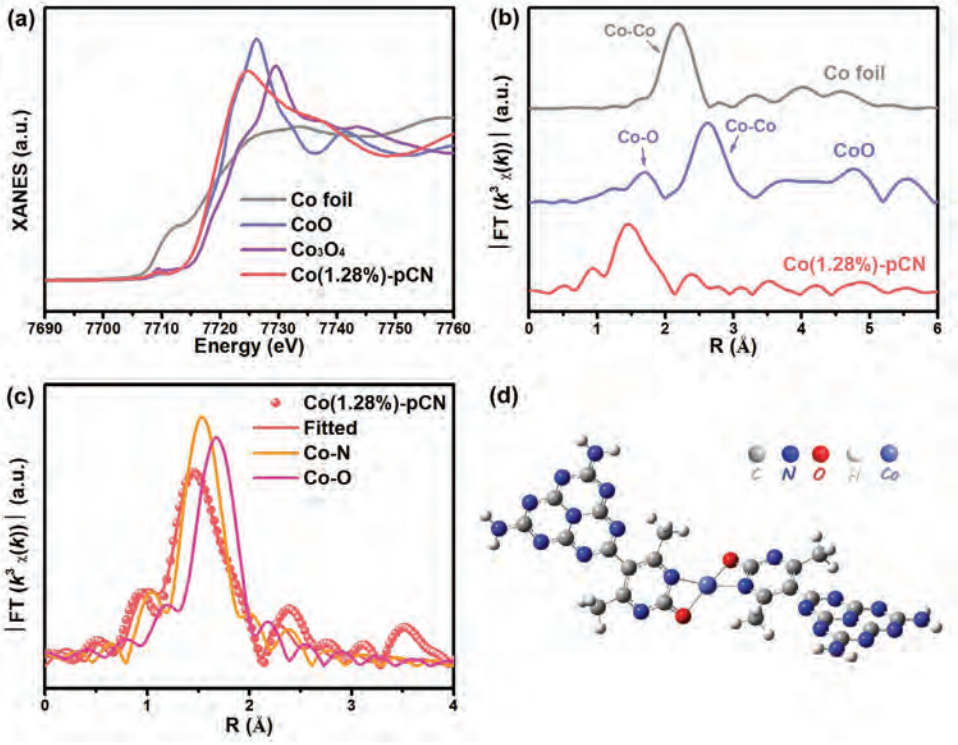

Figure 3. a) Co *k* edge XANES spectra of Co foil, CoO, Co_3O_4, and Co(1.28%)–pCN. b) Corresponding Fourier transform spectra of Co foil, CoO, and Co(1.28%)–pCN. c) EXAFS *r* space-fitting curve of Co(1.28%)–pCN (Insert: *k* space-fitting curve of Co(1.28%)–pCN). d) Optimized DFT calculation model of Co(1.28%)–pCN.

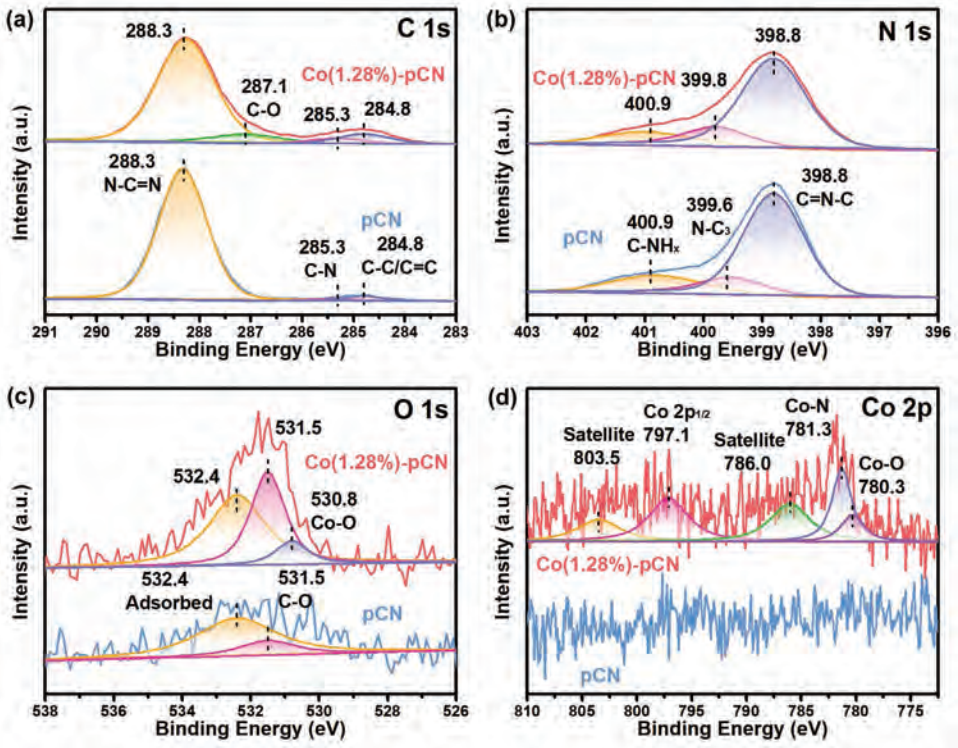

Figure 4. XPS spectra for pCN and Co(1.28%)–pCN: a) C 1s, b) N 1s, c) O 1s, and d) Co 2p.

lone pair of electrons on the nitrogen atom transfer to the Co atom through the coordinative Co—N bond. In O 1s spectrum of pCN (Figure 4c), the peaks at 532.4 and 531.5 eV are assigned to adsorbed CO_2 or H_2O and C—O, respectively.[29] Compared to pCN, these two peaks in Co(1.28%)–pCN are strengthened owing to the incorporation of HDMP. And a new peak at 530.8 eV is emerged in Co(1.28%)–pCN, which can be assigned to the Co—O bond.[30] Moreover, the Co 2p band is observed only with the Co(1.28%)–pCN (Figure 4d). The Co 2p spectrum of Co(1.28%)–pCN can be deconvoluted into two pairs of peaks, where the two pairs of peaks at 803.5/797.1 and 786.0/781.3/780.3 eV correspond to Co $2p_{1/2}$ and Co $2p_{3/2}$, respectively. The sharp peaks at 781.3 and 780.3 eV are attributed to Co—N and Co—O bonds, respectively.[31] The above X-ray adsorption spectroscopy (XAS) and XPS results corroborate the distribution of Co atoms on the pCN support, which are stabilized by the strong interactions of Co—O/N bonds.

Light-harvesting ability of the photocatalyst is an important factor affecting its photocatalytic performance. As displayed by the ultraviolet–visible diffuse reflectance spectra (UV–vis DRS) in Figure S5a (Supporting Information), the introduction of Co atoms causes an enhanced optical absorption for pCN in the visible light region because of the optical absorption of surface Co atoms. This change is also evidenced by the physical appearance changes. With the increase of Co concentration, the color of the sample changes from faint yellow to brown (inset image of Figure S5a, Supporting Information). The bandgap energy (E_g) is calculated by the Kubelka–Munk method. Based upon the Tauc plots in Figure S5b (Supporting Information), the E_g values of pCN and Co(1.28%)–pCN are deduced to be 2.62 and 1.91 eV, respectively. In addition, the potentials of the valence band (VB) are estimated to be 1.81 and 1.26 V for pCN and Co(1.28%)—pCN according to the VB-XPS spectra (Figure S5c, Supporting Information). Therefore, the conduction band (CB) potentials of pCN and Co(1.28%)–pCN are evaluated to be –0.81 and –0.65 V from the formula $E_{CB} = E_{VB} - E_g$ (E_{CB} and E_{VB} indicate the CB and VB energies), and the detailed band structure alignments is displayed in Figure S5d (Supporting Information).

Except for the optical absorption, Co(1.28%)–pCN also has more unpaired electrons in the aromatic system than pCN, as verified by electron spin resonance (ESR) spectra displayed in **Figure 5**a. Obviously, both pCN and Co(1.28%)–pCN exhibit a single Lorentzian line centered at a *g*-value of 2.003

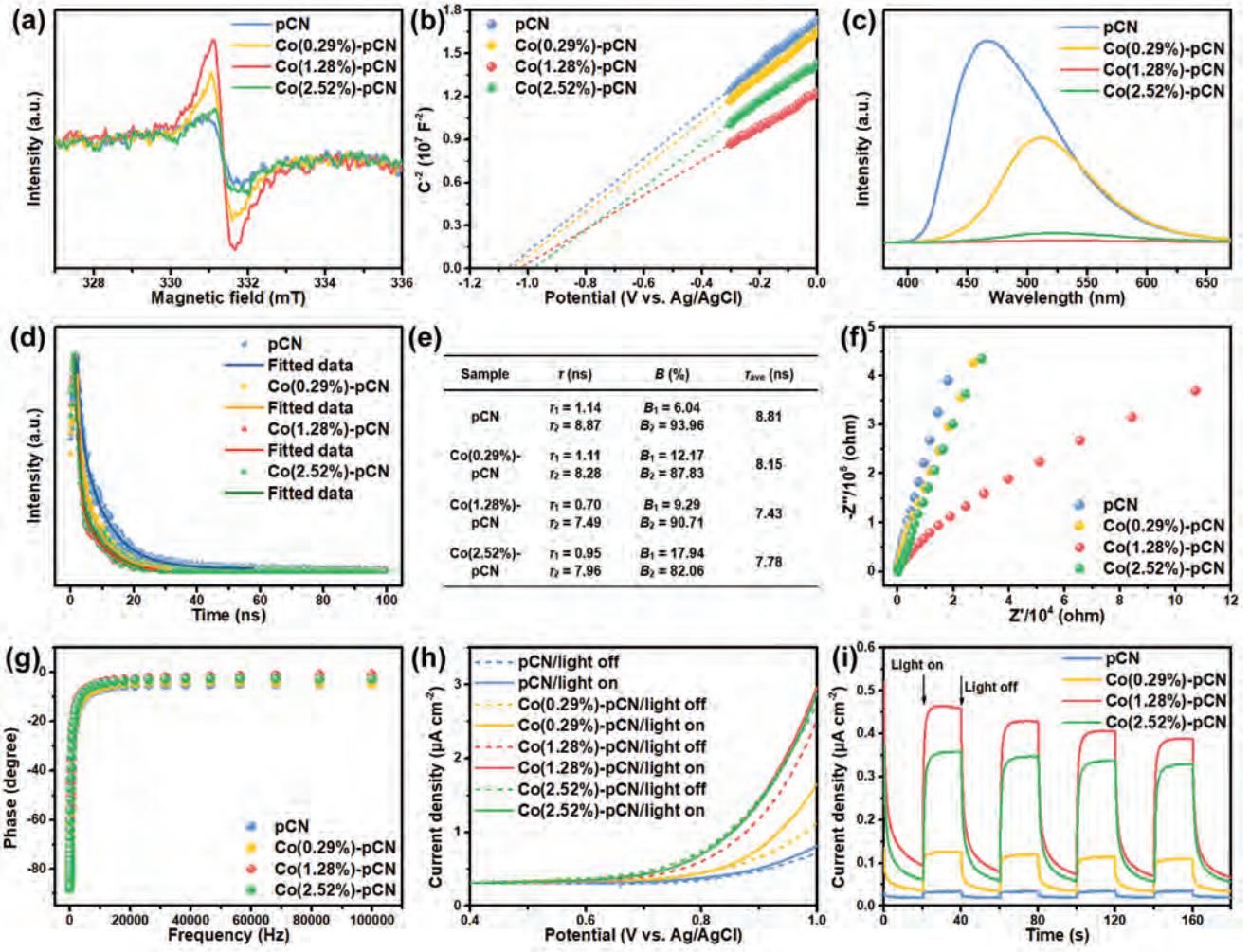

Figure 5. a) ESR spectra, b) Mott–Schottky curves, c) PL spectra, d) TRPL spectra, e) TRPL lifetimes, f) Nyquist plots of EIS, g) Bode phase spectra, h) LSV curves, and i) transient photocurrent curves of the samples.

owing to the unpaired electrons on the carbon atoms of the π-conjugated aromatic rings.[32] But the ESR intensity of Co(1.28%)–pCN is increased significantly compared to that of pCN, suggesting the enhanced delocalization of π system and the improved electron mobility. Thus, the density of charge carriers will be increased, which can be evidenced by the Mott–Schottky analysis. As displayed in Figure 5b, both pCN and Co(1.28%)–pCN present positive slopes, suggesting that they are n-type semiconductors with electron conduction. Accordingly, the charge carrier density (N_D) can be calculated from the slope of the Mott–Schottky curve using Equation (1)[33]

$$N_D = \frac{2}{q\varepsilon\varepsilon_0}\frac{dE}{d(1/C^2)} = \frac{2}{q\varepsilon\varepsilon_0}\frac{1}{\text{slope}} \quad (1)$$

where q represents the electronic charge (1.602×10^{-19} C), and ε and ε_0 are the dielectric constants of carbon nitride (5.25) and the permittivity in vacuum (8.85×10^{-14} F cm^{-2}). On the basis of the slopes of the Mott–Schottky curves, the N_D values of pCN and Co(1.28%)–pCN are computed to be 1.68×10^{24} and 1.88×10^{24} cm^{-3}, respectively. The larger carrier density in the Co(1.28%)–pCN will contribute to the participation of free charges in photocatalytic reaction.

Next, the photogenerated charge-transfer behaviors, which are the key factors in determining the photocatalytic activity, are investigated. The separation and recombination efficiency of the photogenerated electron–hole pairs are analyzed by photoluminescence (PL) and time-resolved photoluminescence (TRPL) spectra. As displayed in Figure 5c, compared with pCN, the Co(1.28%)–pCN shows significant decrease of the PL intensity, suggesting a larger barrier to charge recombination in Co(1.28%)–pCN. The emission peak is redshifted, which is attributed to the extended π-conjugation induced by HDMP.[34] In order to investigate the lifetimes of photogenerated charges and to further validate the processes of charge separation, the TRPL decay curves are collected on pCN and Co(1.28%)–pCN, as shown in Figure 5d. The TRPL decay curves are fitted biexponentially using Equation (2)[35]

$$R(t) = B_1 \exp\left(-\frac{t}{\tau_1}\right) + B_2 \exp\left(-\frac{t}{\tau_2}\right) \quad (2)$$

where B_1 and B_2 represent the normalized amplitudes of each decay component, and τ_1 and τ_2 are values of the lifetime components, respectively. All of the fitting TRPL decay data are listed in Figure 5e. The average lifetime (τ_{ave}) is calculated from the two lifetime components using Equation (3)

$$\tau_{ave} = \frac{B_1\tau_1^2 + B_2\tau_2^2}{B_1\tau_1 + B_2\tau_2} \quad (3)$$

From Equation (3), the average lifetimes of pCN and Co(1.28%)–pCN are calculated to be 8.81 and 7.43 ns, respectively. In comparison to pCN, the lifetime of Co(1.28%)–pCN is decreased, suggesting the faster quenching of the Co(1.28%)–pCN luminescence. Generally, the fast quenching is because of the improved charge separation or stronger nonradiative transitions. Therefore, the decreased lifetime in Co(1.28%)–pCN is indicative of the enhanced dissociation and transfer efficiency of photogenerated excitons.[14b,36]

The transfer ability of photogenerated charge carriers is further studied by the photo-electrochemistry. First, the electrochemical impedance spectroscopy (EIS) analysis is performed to investigate the electronic conductivity of the samples. As shown by EIS Nyquist plots in Figure 5f, the electronic resistance of Co(1.28%)–pCN is smaller than that of pCN, suggesting much lower electron-transfer resistance. Meanwhile, the bode phase spectra (Figure 5g) show that the frequency peak of Co(1.28%)–pCN shifts slightly to a lower frequency compared with pCN, which indicates a more rapid electron-transfer process on Co(1.28%)–pCN. In addition, the linear sweep voltammetry (LSV) curves and transient photocurrent response curves are collected. As exhibited in Figure 5h, the current density of pCN and Co(1.28%)–pCN are 0.72 and 2.52 μA cm^{-2} under dark and 0.81 and 2.96 μA cm^{-2} under light at 1.0 V versus Ag/AgCl, respectively. The increased current density in Co(1.28%)–pCN suggests its enhanced charge separation and accelerated charge transfer. Figure 5i displays the comparison of the transient photocurrent responses of pCN and Co(1.28%)–pCN. When the light is switched on, the photocurrents of the samples increase to their maximum level and keep nearly unchanged. Then the photocurrents decrease to the background value when the light is switched off. It is obvious that Co(1.28%)–pCN presents a larger photocurrent than pCN, indicating that Co(1.28%)–pCN possesses superior ability for the separation and transfer of the photogenerated electron–hole pairs. Overall, these results demonstrate well that the light-harvesting ability, charge transfer, and separation efficiency of pCN are improved because of the implantation of single-atom cobalt. Therefore, better photocatalytic performance can be anticipated.

The photocatalytic performance of the Co–pCN samples is evaluated by the degradation of OTC under visible light irradiation ($\lambda > 420$ nm). As shown in Figure S6 (Supporting Information), the adsorption ability of the samples for OTC increases with the increase of single-atom cobalt content, while the difference in BET surface area of these samples is not obvious. This result indicates that the single-atom cobalt can promote the adsorption of OTC, which will be beneficial to the OTC degradation. The photocatalytic degradation efficiency (DE, %) for OTC is calculated using Equation (4)

$$DE(\%) = \left(1 - \frac{C_t}{C_0}\right) \times 100\% \quad (4)$$

where C_t is the concentration of OTC solution after t minutes of photocatalytic reaction and C_0 is the initial concentration of OTC. As shown in **Figure 6**a, no obvious change in OTC concentration can be observed in the absence of photocatalyst, suggesting that the photolysis plays a negligible role in OTC degradation. pCN presents 33.2% degradation efficiency for OTC after 40 min of photocatalytic reaction. Compared to pCN, the OTC degradation efficiencies of Co-incorporated samples are all significantly enhanced. Among the Co-incorporated samples, the Co(1.28%)–pCN sample exhibits the highest activity for OTC degradation (75.7%). The time-dependent UV–vis spectra of OTC solution over the Co(1.28%)–pCN photocatalyst (Figure S7, Supporting

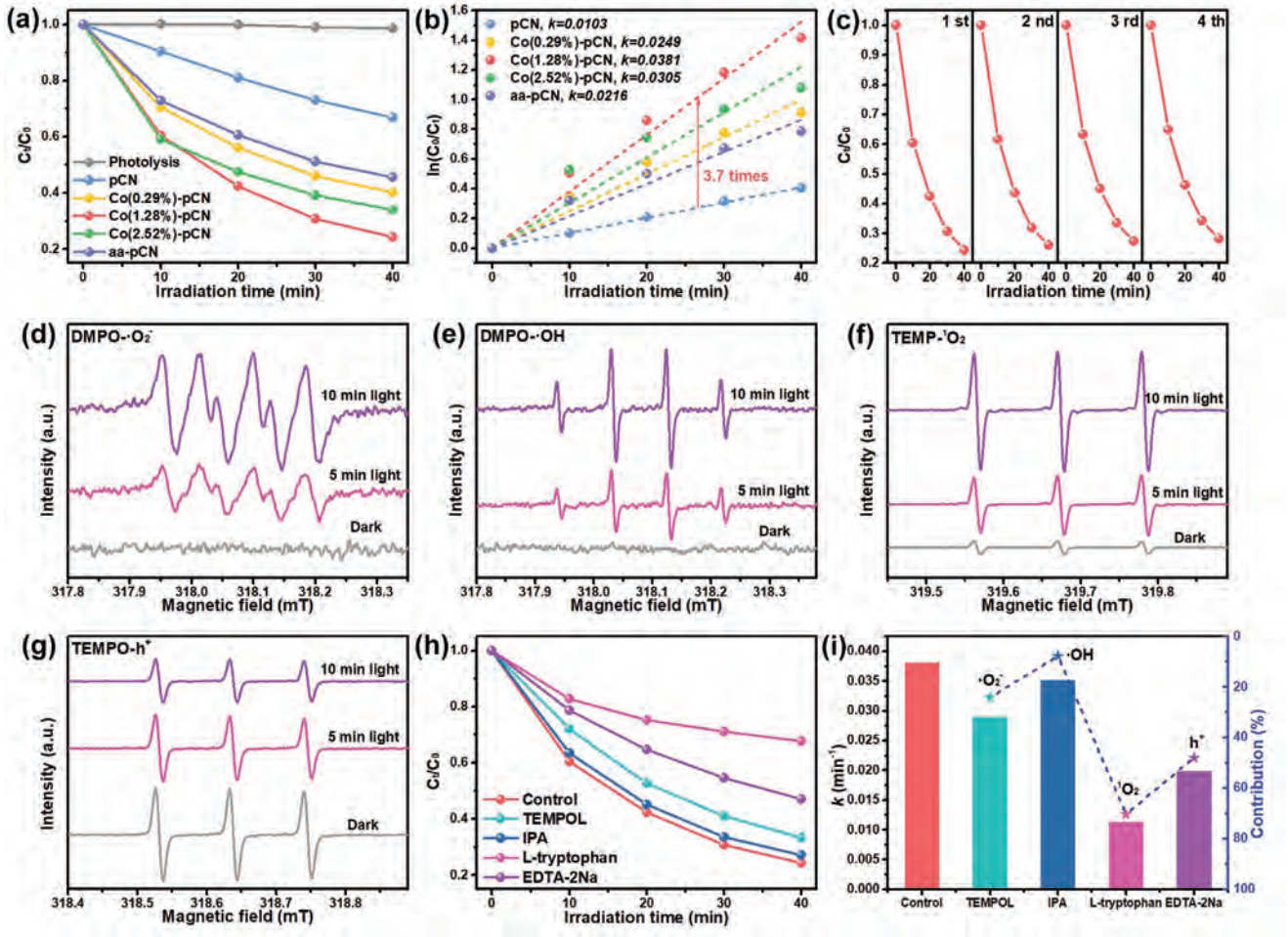

Figure 6. a) Photocatalytic degradation efficiency of OTC over different samples under visible light irradiation ($\lambda > 420$ nm). b) Pseudo-first-order kinetic fitting curves and the corresponding kinetic constants. c) Four cycles of degradation of OTC by Co(1.28%)–pCN. ESR spectra of the d) DMPO–•O_2^- adduct, e) DMPO–•OH adduct, f) TEMP–$^1O_2$ adduct, and g) TEMPO–h^+ adduct for Co(1.28%)–pCN under visible light irradiation. h) Photocatalytic degradation curves of OTC with different quenchers over Co(1.28%)–pCN under visible light irradiation and i) the corresponding kinetic constants as well as the relative contributions of different quenchers.

Information) apparently demonstrate that the absorbance of OTC characteristic absorption peak (353 nm) decreases with the prolonged irradiation time. However, as the content of single-atom cobalt increases, the photocatalytic activity of the sample (Co(2.52%)–pCN) is decreased due to the rapid recombination of photogenerated charges. Interestingly, the aa-pCN shows some improvement in photocatalytic degradation of OTC, while the activity improvement is more pronounced in the presence of single-atom cobalt, implying that the single-atom cobalt is crucial for high photocatalytic performance. Moreover, the curves of $\ln(C_0/C_t)$ versus t over the samples show a linear relationship (Figure 6b), which is in agreement with the pseudo-first-order model. Thus, the apparent rate constants (k) for OTC degradation over the samples can be deduced by Equation (5)

$$k = \frac{\ln(C_0/C_t)}{t} \tag{5}$$

The k value of the Co(1.28%)–pCN is 0.038 min^{-1}, which is 3.7 times than that of pCN. These results suggest that the single-atom cobalt can highly efficient enhance the photocatalytic performance of pCN. The photocatalytic stability of the Co(1.28%)–pCN sample is studied by cyclic photocatalytic OTC degradation reactions and a series of characterizations. As displayed in Figure 6c, the Co(1.28%)–pCN photocatalyst still presents high photocatalytic activity for OTC degradation in the subsequent runs and shows no noticeable decrease after four runs. Besides, the XPS, XRD, Raman, and ATR–FTIR spectra of the Co(1.28%)–pCN sample (Figure S8, Supporting Information) remain almost unchanged after the photocatalytic reaction, further verifying the physicochemical stability of the Co (1.28%)–pCN photocatalyst. Meanwhile, the photocatalytic degradation activity of Co–pCN is higher than most of other pCN-based photocatalysts reported previously (**Table 1**), demonstrating that Co–pCN is a promising photocatalyst for degradation of organic pollutants.

For deeply understanding the transformation pathways of OTC degradation over Co(1.28)–pCN, the degradation intermediates of OTC are identified by the liquid chromatography coupled with tandem mass spectrometry (LC/MS–MS)

Table 1. Comparison with other pCN-based photocatalysts for degradation.

Photocatalysts	Pollutant concentration [mg L^{-1}]	Dosage [g L^{-1}]	Light source	k[a] [min^{-1}]	Ref. (year)
β-Bi_2O_3@g–C_3N_4	TC[b] (10)	0.50	250 W XL[c] ($\lambda > 420$ nm)	0.031	[37] (2018)
Co_3O_4/g-C_3N_4	TC (10)	0.50	500 W XL ($\lambda > 420$ nm)	0.010	[38] (2018)
γ-Fe_2O_3/g-C_3N_4	TC (10)	0.50	500 W XL ($\lambda > 420$ nm)	0.014	[39] (2018)
Co_3O_4@CoO/g-C_3N_4	TC (10)	0.60	500 W XL ($\lambda > 420$ nm)	0.021	[40] (2019)
h-BN/g-C_3N_4	TC (10)	1.00	300 W XL ($\lambda > 420$ nm)	0.028	[41] (2018)
CDs[d]/g-C_3N_4/MoO_3	TC (20)	0.60	350 W XL ($\lambda > 420$ nm)	0.023	[42] (2018)
KMCN[e]	TC (20)	1.00	300 W XL ($\lambda > 420$ nm)	0.028	[43] (2018)
HTCN-C[f]	TC (20)	1.00	300 W XL ($\lambda > 420$ nm)	0.029	[44] (2019)
CNF[g]	TC (21)	0.50	300 W XL ($\lambda > 420$ nm)	0.014	[45] (2018)
BPTCN[h]	OTC (10)	0.60	300 W XL ($\lambda > 420$ nm)	0.028	[46] (2020)
BNQDs[i]/UPCN[j]	OTC (10)	1.00	300 W XL ($\lambda > 420$ nm)	0.031	[47] (2019)
OCN[k]	OTC (20)	1.00	300 W XL ($\lambda > 420$ nm)	0.016	[48] (2020)
Co—pCN	OTC (20)	0.30	300 W XL ($\lambda > 420$ nm)	0.038	This work

[a] k is apparent rate constant; [b] TC is tetracycline; [c] XL is the xenon lamp; [d] CDs is carbon dots; [e] KMCN is K-doped porous ultrathin g-C_3N_4; [f] HTCN-C is S doped carbon quantum dots/hollow tubular g-C_3N_4; [g] CNF is polymeric carbon nitride foam; [h] BPTCN is black phosphorus quantum dots/tubular g-C_3N_4; [i] BNQDs is boron nitride quantum dots; [j] UPCN is ultrathin porous g-C_3N_4; [k] OCN is oxygen-substituted ultrathin porous g-C_3N_4.

technology, and the results are shown in Figure S9 and Table S2 (Supporting Information). On the basis of the detected intermediates and related reports,[49] the proposed degradation process is displayed in Scheme S1 (Supporting Information). First OTC (m/z = 461.1) is decomposed to OTC 1 (m/z = 382.9) through the deamidation, dehydroxylation, and dehydration. OTC 1 is then fragmented into OTC 4 (m/z = 279.1), and transformed to OTC 6 (m/z = 262.9) via dehydroxylation. Meanwhile, OTC also can be decomposed to OTC 2 (m/z = 362.3) via the *N*-demethylation, decarbonylation, dehydroxylation, and deamidation. And due to the demethylation, decarbonylation, and dehydroxylation, OTC 2 is transformed to OTC 3 (m/z = 318.3). Then OTC 3 is decomposed to OTC 5 (m/z = 274.5) via deamination and dehydroxylation. Subsequently, these intermediates are oxidized to produce opening ring products including OTC 7 (m/z = 198.1), OTC 8 (m/z = 194.0), OTC 9 (m/z = 180.0), and OTC 10 (m/z = 143.0). Lastly, these ring-opening products are oxidized into CO_2 and H_2O. The total organic carbon (TOC) removal efficiency is investigated to assess the mineralization ability of Co(1.28%)–pCN for OTC. As exhibited in Figure S10 (Supporting Information), the TOC removal efficiency in OTC aqueous solution is 18.3% in 40 min under visible light irradiation, further confirming the enhanced photocatalytic performance for Co(1.28%)–pCN.

Furthermore, the generation of reactive species over the Co(1.28%)–pCN photocatalysts is probed by the 5,5-dimethyl-1-pyrroline *N*-oxide (DMPO), 2,2,6,6-tetramethylpiperidine (TEMP), and 2,2,6,6-tetramethylpiperidine-1-oxyl (TEMPO) spin-trapping ESR technique. Figure 6d,e shows that no ESR signals are monitored in the dark, but two obvious ESR signals are recorded under visible light irradiation. The intensity ratios of these two signals are 1:1:1:1 and 1:2:2:1, which are attributed to the DMPO–•O_2^- and DMPO–•OH adducts, respectively. Meanwhile, a three-line ESR signal of TEMP–$^1O_2$ adduct with an intensity ratio of 1:1:1 is observed (Figure 6f). The signal of TEMP–$^1O_2$ adduct in the dark may be originated from the energy transfer of molecule oxygen.[50] Besides, Figure 6g displays the signal of TEMPO–h^+ adduct in the dark and under visible light irradiation, which possesses three peaks with an intensity of 1:1:1. The ESR signal of TEMPO–h^+ adduct decreases upon visible light irradiation, indicating the generation of photogenerated holes.[51] With the prolonged irradiation time, the signal intensity of all the four adducts changes, demonstrating their continuous generation by the Co(1.28%)–pCN photocatalyst during the irradiation process. In order to clarify the contribution of specific reactive species generated in the Co(1.28%)–pCN photocatalytic system for OTC degradation, reactive species trapping experiments are carried out by adding quenchers. The quenchers for •O_2^-, •OH, $^1O_2$, and h^+ are 4-hydroxy-2,2,6,6-tetramethylpiperidinyloxy (TEMPOL), isopropanol (IPA), L-tryptophan, and ethylenediaminetetraacetic acid disodium (EDTA-2Na), respectively. As shown in Figure 6h, different quenchers have different effects on OTC degradation in the presence of Co(1.28%)–pCN photocatalyst. Specifically, the degradation efficiency of OTC after 40 min of irradiation on solutions containing TEMPOL, IPA, L-tryptophan, and EDTA-2Na are 66.6%, 72.9%, 32.4%, and 52.9%, respectively. And the corresponding apparent rate constants are 0.029, 0.035, 0.011, and 0.020 min^{-1}, respectively (Figure 6i). The relative contributions of •O_2^-, •OH, $^1O_2$, and h^+ to the overall OTC degradation can be deduced by Equations (6)–(9)

$$R_{\cdot O_2^-} = \frac{k_{\cdot O_2^-}}{k} \approx \frac{(k - k_{\mathrm{TEMPOL}})}{k} \quad (6)$$

$$R_{\mathrm{OH}} = \frac{k_{\cdot \mathrm{OH}}}{k} \approx \frac{(k - k_{\mathrm{IPA}})}{k} \quad (7)$$

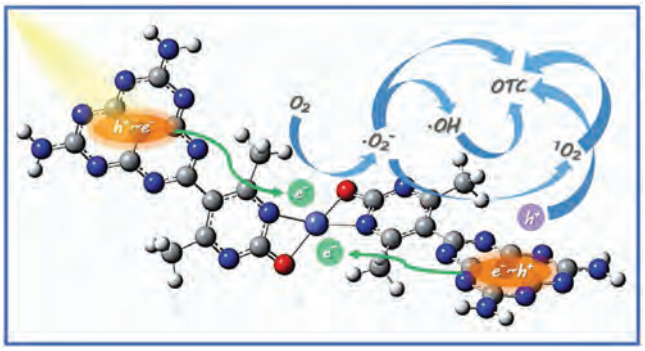

Scheme 1. The proposed photocatalytic degradation mechanism of OTC in Co–pCN.

$$R_{^1O_2} = \frac{k_{^1O_2}}{k} \approx \frac{(k - k_{\text{L-tryptophan}})}{k} \tag{8}$$

$$R_{h^+} = \frac{k_{h^+}}{k} \approx \frac{(k - k_{\text{EDTA-2Na}})}{k} \tag{9}$$

Accordingly, they are 23.7%, 7.9%, 71.1%, and 47.4%, respectively. Because of the complex radical chemistry involved in the photocatalytic reaction, the sum of the contributions of these four reactive species exceeds 100%. These results demonstrate that $^1O_2$, h^+, and $\bullet O_2^-$ play significant roles in the Co(1.28%)–pCN photocatalytic system for OTC degradation. In addition, the major reactive species in the OTC degradation driven by pure pCN are identified to be $\bullet O_2^-$, $^1O_2$, and h^+ (Figure S11a, Supporting Information). And the relative contributions of $\bullet O_2^-$, $^1O_2$, h^+, and •OH to the overall OTC degradation are estimated to be 64.6%, 44.9%, 35.1%, and 6.4%, respectively (Figure S11b, Supporting Information). After single-atom cobalt incorporation, the most primary reactive specie changes from $\bullet O_2^-$ to $^1O_2$, indicating that the single-atom cobalt may favor the formation of $^1O_2$.

On the basis of the above results and discussion, the mechanism of OTC degradation in the Co–pCN photocatalyst can be proposed, as shown in **Scheme 1**. Under visible light irradiation ($\lambda > 420$ nm), the Co–pCN is excited to generate electrons (e^-) and holes (h^+) (Equation (10)). As the CB potential of Co(1.28%)–pCN (–0.65 V vs normal hydrogen electrode (NHE)) is lower than the redox potential of $O_2/\bullet O_2^-$ (–0.33 V vs NHE), the photogenerated electrons on the CB can be captured by molecular oxygen to form $\bullet O_2^-$ (Equation (11)). Furthermore, $\bullet O_2^-$ can, respectively, react with h^+ to form $^1O_2$ (Equation (12)), and react with e^- and H^+ to form •OH (Equations (13) and (14)). The generated reactive species (h^+, $\bullet O_2^-$, $^1O_2$, and •OH) will then react with the OTC molecule, leading to its degradation (Equation (15))

$$\text{Co-pCN} + h\nu \rightarrow \text{Co-pCN}\left(e^- + h^+\right) \tag{10}$$

$$e^- + O_2 \rightarrow \cdot O_2^- \tag{11}$$

$$\cdot O_2^- + h^+ \rightarrow {}^1O_2 \tag{12}$$

$$\cdot O_2^- + e^- + 2H^+ \rightarrow H_2O_2 \tag{13}$$

$$H_2O_2 + e^- \rightarrow OH^- + \cdot OH \tag{14}$$

$$\left(h^+, \cdot O_2^-, {}^1O_2, \cdot OH\right) + \text{OTC} \rightarrow \text{products} \tag{15}$$

3. Conclusion

In conclusion, a simple in situ growth strategy is developed to implant single-atom cobalt in pCN by the bidentate ligand. HAADF-STEM images demonstrate that the Co atoms are atomically dispersed in pCN. EXAFS analysis further indicates that the single-atom cobalt is immobilized on pCN by covalently forming a Co—O bond and a Co—N bond. Benefiting from the extended optical absorption in the visible region, increased electron density, and accelerated separation and transfer of charge carriers, the Co–pCN photocatalysts present excellent photocatalytic performance for OTC degradation under visible light irradiation ($\lambda > 420$ nm). The apparent rate constant of OTC degradation for optimal sample (Co(1.28%)–pCN) is 0.038 min^{-1}, which is about 3.7 times than that of pristine pCN. This work develops a novel process to synthesize single-atom-modified pCN and provides a green and highly efficient strategy for the OTC removal.

4. Experimental Section

Preparation of Samples: Co–pCN was prepared via thermal polymerization of urea and cobalt(II) acetylacetonate. Typically, 10 g of urea and a certain amount of cobalt(II) acetylacetonate (0, 0.01, 0.05, and 0.1 g) were added into an agate mortar and ground to achieve complete homogeneity. Then, the obtained powders were transferred to a covered crucible and calcined at 550 °C for 2 h with the heating rate of 5 °C min^{-1}, followed by cooling to room temperature naturally. Finally, the product was washed with deionized water and dried at 60 °C for 12 h. The contents of cobalt in pCN were determined by the inductively coupled plasma mass spectrometry (ICP-MS, Agilent 7800) method to be 0.29, 1.28, and 2.52 wt%. And the samples were denoted as Co(0.29%)–pCN, Co(1.28%)–pCN, and Co(2.52%)–pCN, respectively. Besides, the aa-pCN was prepared for solid-state ^{13}C NMR spectra analysis. The added molar amount of acetylacetone and heating process were consistent with the preparation of Co(1.28%)–pCN.

Characterization: Solid-state ^{13}C NMR spectra were obtained with cross-polarization magic angle spinning on a Bruker Avance III 600 spectrometer. XRD patterns were recorded on a Bruker D8 Advance diffractometer with Cu Kα radiation. Raman tests were performed on Horiba Jobin Yvon LabRAM HR800 Raman spectroscopy with a He–Cd laser excitation at 325 nm. ATR-FTIR spectra were acquired on a Thermo Nicolet 5700 spectrophotometer. N_2 adsorption–desorption isotherms and pore size distribution curves were investigated using the BET method on a Micromeritics ASAP 2020 HD88 instrument. SEM images were obtained on a Zeiss Sigma HD electron microscope. TEM and EDS mapping images were collected on an FEI Tecnai G2 F20 S-TWIN electron microscope. HAADF-STEM images were collected on a Cs-corrected FEI Titan G2 60–300 electron microscope. XAS of Co K-edge was recorded on the beamline BL01C1 in National Synchrotron Radiation Research Center (NSRRC), and technical support was provided by Ceshigo Research Service "www.ceshigo.com." The radiation was monochromatized by a Si (111) double-crystal monochromator. The data of XANES and EXAFS were analyzed by Athena software. XPS spectra were acquired on a Thermo Escalab 250Xi spectrometer with monochromatized Al Kα line

source (150 W). UV–vis DRS were collected on a PerkinElmer Lambda 750 UV/vis/NIR spectrometer. ESR spectra were measured on a JEOL JES-FA200 spectrometer at room temperature. PL emission spectra were recorded on a PerkinElmer LS-55 fluorescence spectrophotometer with an excitation wavelength of 350 nm. TRPL decay curves were acquired from an FLS 980 fluorescence lifetime spectrophotometer.

Theoretical Computation: Gaussian program was employed for DFT calculations. Geometry optimization was performed at B3LYP-D3BJ/def2-SVP level.

Photo-Electrochemical Measurement: The photo-electrochemical measurements were conducted on a Chenhua CHI 760E electrochemical workstation using a standard three-compartment electrochemical cell. The platinum foil and Ag/AgCl electrode were used as the counter and reference electrodes, respectively. The working electrode was prepared as follows: 5 mg of the sample was dispersed into 1 mL of 10% nafion solution under ultrasonication to get a slurry. 100 µL of the slurry was then coated on a fluorine-doped tin oxide (FTO) glass (1 cm × 2 cm) with an effective working area of 1 cm^2. After drying at 60 °C for 2 h, the working electrode was calcined at 120 °C for 1 h to enhance adhesion. 0.2 M Na_2SO_4 aqueous solution was employed as the electrolyte. A 300 W xenon lamp (PLS-SXE300/300UV, Perfect Light) equipped with a 420 nm cutoff filter was used to produce light source. Mott–Schottky plots were collected at the frequency of 1000 Hz. EIS was obtained at an applied voltage of 0.15 V with an amplitude of 0.005 V. LSV curves were conducted at the scanning speed of 0.02 V s^{-1}. Transient photocurrent response curves were recorded at an applied voltage of 0 V with the light on or off.

Photocatalysis Experiment: The photocatalytic performance of the samples was assessed by the degradation of OTC under visible light irradiation ($\lambda > 420$ nm). Typically, 30 mg of the photocatalyst was added to 100 mL of 20 mg L^{-1} OTC aqueous solution. Prior to irradiation, this suspension was magnetically stirred in the darkness for 30 min to establish the adsorption–desorption equilibrium of the OTC on the photocatalyst surface. Then, the suspension was irradiated under a 300 W xenon lamp (PLS-SXE300/300UV, Perfect Light) equipped with a 420 nm cutoff filter. At the given irradiation time intervals, 3 mL of the specimen was taken out and centrifuged to separate the photocatalyst powders. The concentration of OTC aqueous solution was determined using a Shimadzu UV-2700 spectrophotometer at 353 nm by measuring its absorbance. The TOC contents were analyzed by a Shimadzu TOC-VCPH analyzer. The degradation intermediates of OTC were analyzed by the LC-MS/MS technology, and the specific method was provided in the Supporting Information. To evaluate the stability of the photocatalyst, the photocatalyst powders were collected via vacuum filtration after one trial washed by deionized water and ethanol, and dried for the cycle experiment.

Reactive Species Examination: ESR spin-trapping technique was utilized to detect reactive species generated in the photocatalytic system. DMPO was used as the trapping reagent for $\bullet O_2^-$ and •OH; TEMP was used as the trapping reagent for $^1O_2$; and TEMPO was used as the trapping reagent for h^+. Furthermore, chemical quenchers were added into the experimental solutions to investigate the contribution of specific reactive species to OTC degradation. The quenching agents for $\bullet O_2^-$, •OH, $^1O_2$, and h^+ were TEMPOL (5×10^{-3} M), IPA (5×10^{-3} M), L-tryptophan (5×10^{-3} M), and EDTA-2Na (5×10^{-3} M), respectively.

Supporting Information

Supporting Information is available from the Wiley Online Library or from the author.

Acknowledgements

This study was financially supported by the Program for the National Natural Science Foundation of China (Grant Nos. 51521006, 51879101, 51579098, 51779090, 51709101, and 51809090), the Three Gorges Follow-up Research Project (2017HXXY-05), the National Program for Support of Top-Notch Young Professionals of China (2014), the Program for Changjiang Scholars and Innovative Research Team in University (IRT-13R17), Hunan Provincial Science and Technology Plan Project (2018SK20410, 2017SK2243, and 2016RS3026), Postgraduate Scientific Research Innovation Project of Hunan Province (CX20190293), the Natural Science Foundation of Hunan Province, China (Grant No. 2019JJ50077), and the Fundamental Research Funds for the Central Universities (Grant Nos. 531119200086, 531118010114, 531107050978, and 541109060031).

Conflict of Interest

The authors declare no conflict of interest.

Keywords

carbon nitride, in situ growth, oxytetracycline degradation, photocatalysis, single atoms

Received: March 12, 2020
Revised: May 8, 2020
Published online:

[1] a) Q. Zhang, G. Ying, C. Pan, Y. Liu, J. Zhao, *Environ. Sci. Technol.* **2015**, *49*, 6772; b) S. Tian, C. Zhang, D. Huang, R. Wang, G. Zeng, M. Yan, W. Xiong, C. Zhou, M. Cheng, W. Xue, X. Y. Yang, W. Wang, *Chem. Eng. J.* **2020**, *389*, 123423; c) M. Jia, Z. Yang, H. Xu, P. Song, W. Xiong, J. Cao, Y. Zhang, Y. Xiang, J. Hu, C. Zhou, Y. Yang, W. Wang, *Chem. Eng. J.* **2020**, *388*, 124388.

[2] a) R. Ding, W. Yan, Y. Wu, Y. Xiao, H. Gang, S. Wang, L. Chen, F. Zhao, *Water Res.* **2018**, *143*, 589; b) H. Yi, M. Yan, D. Huang, G. Zeng, C. Lai, M. Li, X. Huo, L. Qin, S. Liu, X. Liu, *Appl. Catal., B* **2019**, *250*, 52.

[3] a) H. Wang, M. Zhang, X. He, T. Du, Y. Wang, Y. Li, T. Hao, *Water Res.* **2019**, *160*, 197; b) S. Ye, M. Yan, X. Tan, J. Liang, G. Zeng, H. Wu, B. Song, C. Zhou, Y. Yang, H. Wang, *Appl. Catal., B* **2019**, *250*, 78.

[4] a) M. Yang, M. Gao, M. Hong, G. W. Ho, *Adv. Mater.* **2018**, *30*, 1802894; b) Y. Yang, C. Zhang, C. Lai, G. Zeng, D. Huang, M. Cheng, J. Wang, F. Chen, C. Zhou, W. Xiong, *Adv. Colloid Interface Sci.* **2018**, *254*, 76; c) S. Chen, D. Huang, P. Xu, X. Gong, W. Xue, L. Lei, R. Deng, J. Li, Z. Li, *ACS Catal.* **2020**, *10*, 1024; d) X. Li, Z. Zeng, G. Zeng, D. Wang, R. Xiao, Y. Wang, C. Zhou, H. Yi, S. Ye, Y. Yang, W. Xiong, *J. Colloid Interface Sci.* **2020**, *561*, 501.

[5] a) A. Savateev, I. Ghosh, B. König, M. Antonietti, *Angew. Chem., Int. Ed.* **2018**, *57*, 15936; b) Y. Yang, G. Zeng, D. Huang, C. Zhang, D. He, C. Zhou, W. Wang, W. Xiong, X. Li, B. Li, W. Dong, Y. Zhou, *Appl. Catal., B* **2020**, *272*, 118970; c) C. Zhou, P. Xu, C. Lai, C. Zhang, G. Zeng, D. Huang, M. Cheng, L. Hu, W. Xiong, X. Wen, *Chem. Eng. J.* **2019**, *359*, 186; d) C. Zhou, G. Zeng, D. Huang, Y. Luo, M. Cheng, Y. Liu, W. Xiong, Y. Yang, B. Song, W. Wang, *J. Hazard. Mater.* **2020**, *386*, 121947.

[6] X. Wang, K. Maeda, A. Thomas, K. Takanabe, G. Xin, J. M. Carlsson, K. Domen, M. Antonietti, *Nat. Mater.* **2009**, *8*, 76.

[7] a) W. J. Ong, L. L. Tan, Y. H. Ng, S. T. Yong, S. P. Chai, *Chem. Rev.* **2016**, *116*, 7159; b) J. Cai, J. Huang, S. Wang, J. Iocozzia, Z. Sun, J. Sun, Y. Yang, Y. Lai, Z. Lin, *Adv. Mater.* **2019**, *31*, 1806314; c) G. Zhang, M. Liu, T. Heil, S. Zafeiratos, A. Savateev, M. Antonietti, X. Wang, *Angew. Chem., Int. Ed.* **2019**, *58*, 14950;

d) Y. Li, S. Ouyang, H. Xu, W. Hou, M. Zhao, H. Chen, J. Ye, *Adv. Funct. Mater.* **2019**, *29*, 1901024.
[8] a) Y. Wang, S. Z. F. Phua, G. Dong, X. Liu, B. He, Q. Zhai, Y. Li, C. Zheng, H. Quan, Z. Li, *Chem* **2019**, *5*, 2775; b) L. Lin, Z. Yu, X. Wang, *Angew. Chem.* **2019**, *131*, 6225; c) J. Fu, J. Yu, C. Jiang, B. Cheng, *Adv. Energy Mater.* **2018**, *8*, 1701503; d) P. Qiu, C. Xu, N. Zhou, H. Chen, F. Jiang, *Appl. Catal., B* **2018**, *221*, 27; e) D. He, C. Zhang, G. Zeng, Y. Yang, D. Huang, L. Wang, H. Wang, *Appl. Catal., B* **2019**, *258*, 117957.
[9] a) Z. Chen, S. Pronkin, T. P. Fellinger, K. Kailasam, G. Vilé, D. Albani, F. Krumeich, R. Leary, J. Barnard, J. M. Thomas, *ACS Nano* **2016**, *10*, 3166; b) C. Choi, L. Lin, S. Gim, S. Lee, H. Kim, X. Wang, W. Choi, *ACS Catal.* **2018**, *8*, 4241; c) Y. Zhou, W. Wang, C. Zhang, D. Huang, C. Lai, M. Cheng, L. Qin, Y. Yang, C. Zhou, B. Li, H. Luo, D. He, *Adv. Colloid Interface Sci.* **2020**, *279*, 102144.
[10] X. Wang, X. Chen, A. Thomas, X. Fu, M. Antonietti, *Adv. Mater.* **2009**, *21*, 1609.
[11] a) V. Artero, M. Chavarotkerlidou, M. Fontecave, *Angew. Chem., Int. Ed.* **2011**, *50*, 7238; b) C. Li, X. Tong, P. Yu, W. Du, J. Wu, H. Rao, Z. Wang, *J. Mater. Chem. A* **2019**, *7*, 16622.
[12] a) G. Zhang, C. Huang, X. Wang, *Small* **2015**, *11*, 1215; b) Y. Zhu, T. Wan, X. Wen, D. Chu, Y. Jiang, *Appl. Catal., B* **2019**, *244*, 814; c) F. Zhang, J. Zhang, J. Li, X. Jin, Y. Li, M. Wu, X. Kang, T. Hu, X. Wang, W. Ren, *J. Mater. Chem. A* **2019**, *7*, 6939; d) J. Gu, H. Chen, F. Jiang, X. Wang, L. Li, *Chem. Eng. J.* **2019**, *360*, 1188.
[13] I. F. Teixeira, E. C. Barbosa, S. C. E. Tsang, P. H. Camargo, *Chem. Soc. Rev.* **2018**, *47*, 7783.
[14] a) Y. Li, T. Kong, S. Shen, *Small* **2019**, *15*, 1900772; b) S. Cao, H. Li, T. Tong, H.-C. Chen, A. Yu, J. Yu, H. M. Chen, *Adv. Funct. Mater.* **2018**, *28*, 1802169; c) X. Guo, S. Chen, H. Wang, Z. Zhang, H. Lin, L. Song, T. Lu, *J. Mater. Chem. A* **2019**, *7*, 19831.
[15] W. Liu, L. Cao, W. Cheng, Y. Cao, X. Liu, W. Zhang, X. Mou, L. Jin, X. Zheng, W. Che, Q. Liu, T. Yao, S. Wei, *Angew. Chem., Int. Ed.* **2017**, *56*, 9312.
[16] Y. Cao, S. Chen, Q. Luo, H. Yan, Y. Lin, W. Liu, L. Cao, J. Lu, J. Yang, T. Yao, S. Wei, *Angew. Chem., Int. Ed.* **2017**, *56*, 12191.
[17] P. Huang, J. Huang, S. A. Pantovich, A. D. Carl, T. G. Fenton, C. A. Caputo, R. L. Grimm, A. I. Frenkel, G. Li, *J. Am. Chem. Soc.* **2018**, *140*, 16042.
[18] D. Zhao, C. Dong, B. Wang, C. Chen, Y. Huang, Z. Diao, S. Li, L. Guo, S. Shen, *Adv. Mater.* **2019**, *31*, 1903545.
[19] D. Adsmond, A. Sinha, U. Khandavilli, A. Maguire, S. Lawrence, *Cryst. Growth Des.* **2016**, *16*, 59.
[20] a) Y. Xiao, G. Tian, W. Li, Y. Xie, B. Jiang, C. Tian, D. Zhao, H. Fu, *J. Am. Chem. Soc.* **2019**, *141*, 2508; b) S. Cao, H. Chen, F. Jiang, X. Wang, *Appl. Catal., B* **2018**, *224*, 222.
[21] Y. Wang, F. Silveri, M. K. Bayazit, Q. Ruan, Y. Li, J. Xie, C. R. A. Catlow, J. Tang, *Adv. Energy Mater.* **2018**, *8*, 1801084.
[22] W. Wang, H. Zhang, S. Zhang, Y. Liu, G. Wang, C. Sun, H. Zhao, *Angew. Chem., Int. Ed.* **2019**, *58*, 16644.
[23] N. Meng, J. Ren, Y. Liu, Y. Huang, T. Petit, B. Zhang, *Energy Environ. Sci.* **2018**, *11*, 566.
[24] H. Song, G. Liu, J. Zhang, J. Wu, *Fuel Process. Technol.* **2017**, *156*, 454.
[25] Z. Guo, Y. Xie, J. Xiao, Z. Zhao, Y. Wang, Z. Xu, Y. Zhang, L. Yin, H. Cao, J. Gong, *J. Am. Chem. Soc.* **2019**, *141*, 12005.
[26] Y. Yang, Z. Zeng, G. Zeng, D. Huang, R. Xiao, C. Zhang, C. Zhou, W. Xiong, W. Wang, M. Cheng, *Appl. Catal., B* **2019**, *258*, 117956.
[27] Z. Wei, M. Liu, Z. Zhang, W. Yao, H. Tan, Y. Zhu, *Energy Environ. Sci.* **2018**, *11*, 2581.
[28] X. Tian, Y. Sun, J. He, X. Wang, J. Zhao, S. Qiao, F. Li, *J. Mater. Chem. A* **2019**, *7*, 7628.
[29] S. Yu, J. Li, Y. Zhang, M. Li, F. Dong, T. Zhang, H. Huang, *Nano Energy* **2018**, *50*, 383.
[30] L. Wang, X. Guo, Y. Chen, S. Ai, H. Ding, *Appl. Surf. Sci.* **2019**, *467–468*, 954.
[31] a) M. Zhu, J. Chen, R. Guo, J. Xu, X. Fang, Y. Han, *Appl. Catal., B* **2019**, *251*, 112; b) L. Lin, H. Li, C. Yan, H. Li, R. Si, M. Li, J. Xiao, G. Wang, X. Bao, *Adv. Mater.* **2019**, *31*, 1903470; c) L. Liao, Q. Zhang, Z. Su, Z. Zhao, Y. Wang, Y. Li, X. Lu, D. Wei, G. Feng, Q. Yu, X. Cai, J. Zhao, Z. Ren, H. Fang, F. Robles-Hernandez, S. Baldelli, J. Bao, *Nat. Nanotechnol.* **2014**, *9*, 69; d) Z. Mao, J. Chen, Y. Yang, D. Wang, L. Bie, B. D. Fahlman, *ACS Appl. Mater. Interfaces* **2017**, *9*, 12435; e) Q. Liu, J. Zhang, *Langmuir* **2013**, *29*, 3821.
[32] Z. Chen, T. Fan, X. Yu, Q. Wu, Q. Zhu, L. Zhang, J. Li, W. Fang, X. Yi, *J. Mater. Chem. A* **2018**, *6*, 15310.
[33] L. K. Putri, B.-J. Ng, W.-J. Ong, H. W. Lee, W. S. Chang, S.-P. Chai, *J. Mater. Chem. A* **2018**, *6*, 3181.
[34] a) J. Zhang, G. Zhang, X. Chen, S. Lin, L. Mohlmann, G. Dolega, G. Lipner, M. Antonietti, S. Blechert, X. Wang, *Angew. Chem., Int. Ed.* **2012**, *51*, 3183; b) W. Ho, Z. Zhang, W. Lin, S. Huang, X. Zhang, X. Wang, Y. Huang, *ACS Appl. Mater. Interfaces* **2015**, *7*, 5497; c) J. Li, D. Wu, J. Iocozzia, H. Du, X. Liu, Y. Yuan, W. Zhou, Z. Li, Z. Xue, Z. Lin, *Angew. Chem., Int. Ed.* **2019**, *58*, 1985.
[35] Y. Yu, W. Yan, X. Wang, P. Li, W. Gao, H. Zou, S. Wu, K. Ding, *Adv. Mater.* **2018**, *30*, 1705060.
[36] a) C. Chu, Q. Zhu, Z. Pan, S. Gupta, D. Huang, Y. Du, S. Weon, Y. Wu, C. L. Muhich, E. Stavitski, K. Domen, J. H. Kim, *Proc. Natl. Acad. Sci. USA* **2020**, *117*, 6376; b) Q. Wang, J. Li, X. Tu, H. Liu, M. Shu, R. Si, C. T. J. Ferguson, K. A. I. Zhang, R. Li, *Chem. Mater.* **2020**, *32*, 734; c) Y. Lin, H. Liu, C. Yang, X. Wu, C. Du, L. Jiang, Y. Zhong, *Appl. Catal., B* **2020**, *264*, 118479.
[37] Y. Hong, C. Li, B. Yin, D. Li, Z. Zhang, B. Mao, W. Fan, W. Gu, W. Shi, *Chem. Eng. J.* **2018**, *338*, 137.
[38] H. Wu, C. Li, H. Che, H. Hu, W. Hu, C. Liu, J. Ai, H. Dong, *Appl. Surf. Sci.* **2018**, *440*, 308.
[39] C. Li, S. Yu, H. Che, X. Zhang, J. Han, Y. Mao, Y. Wang, C. Liu, H. Dong, *ACS Sustainable Chem. Eng.* **2018**, *6*, 16437.
[40] J. Zheng, L. Zhang, *Chem. Eng. J.* **2019**, *369*, 947.
[41] L. Jiang, X. Yuan, G. Zeng, Z. Wu, J. Liang, X. Chen, L. Leng, H. Wang, H. Wang, *Appl. Catal., B* **2018**, *221*, 715.
[42] Z. Xie, Y. Feng, F. Wang, D. Chen, Q. Zhang, Y. Zeng, W. Lv, G. Liu, *Appl. Catal., B* **2018**, *229*, 96.
[43] W. Wang, P. Xu, M. Chen, G. Zeng, C. Zhang, C. Zhou, Y. Yang, D. Huang, C. Lai, M. Cheng, *ACS Sustainable Chem. Eng.* **2018**, *6*, 15503.
[44] W. Wang, Z. Zeng, G. Zeng, C. Zhang, R. Xiao, C. Zhou, W. Xiong, Y. Yang, L. Lei, Y. Liu, *Chem. Eng. J.* **2019**, *378*, 122132.
[45] H. Wang, Y. Wu, M. Feng, W. Tu, T. Xiao, T. Xiong, H. Ang, X. Yuan, J. W. Chew, *Water Res.* **2018**, *144*, 215.
[46] W. Wang, Q. Niu, G. Zeng, C. Zhang, D. Huang, B. Shao, C. Zhou, Y. Yang, Y. Liu, H. Guo, W. Xiong, L. Lei, S. Liu, H. Yi, S. Chen, X. Tang, *Appl. Catal., B* **2020**, *273*, 119051.
[47] Y. Yang, C. Zhang, D. Huang, G. Zeng, J. Huang, C. Lai, C. Zhou, W. Wang, H. Guo, W. Xue, *Appl. Catal., B* **2019**, *245*, 87.
[48] H. Guo, C. Niu, C. Feng, C. Liang, L. Zhang, X. Wen, Y. Yang, H. Liu, L. Li, L. Lin, *Chem. Eng. J.* **2020**, *385*, 123919.
[49] a) Y. Yang, Z. Zeng, C. Zhang, D. Huang, G. Zeng, R. Xiao, C. Lai, C. Zhou, H. Guo, W. Xue, *Chem. Eng. J.* **2018**, *349*, 808; b) J. Cao, S. Sun, X. Li, Z. Yang, W. Xiong, Y. Wu, M. Jia, Y. Zhou, C. Zhou, Y. Zhang, *Chem. Eng. J.* **2020**, *382*, 122802; c) Y. Wu, X. Li, Q. Yang, D. Wang, F. Yao, J. Cao, Z. Chen, X. Huang, Y. Yang, X. Li, *Chem. Eng. J.* **2020**, *390*, 124519.
[50] Q. Liu, Y. Guo, Z. Chen, Z. Zhang, X. Fang, *Appl. Catal., B* **2016**, *183*, 231.
[51] T. Xie, Y. Zhang, W. Yao, Y. Liu, H. Wang, Z. Wu, *Catal. Sci. Technol.* **2019**, *9*, 1178.